# Fatigue of wire+arc additive manufactured Ti-6Al-4V in presence of process-induced porosity defects

Emre Akgun [a,b,*], Xiang Zhang [b], Romali Biswal [b], Yanhui Zhang [c], Matthew Doré [c]

[a] National Structural Integrity Research Centre (NSIRC), TWI Ltd, Cambridge CB21 6AL, UK
[b] Faculty of Engineering, Environment and Computing, Coventry University, Coventry CV1 5FB, UK
[c] Materials and Structural Integrity Group, TWI Ltd., Cambridge CB21 6AL, UK

ARTICLE INFO

ABSTRACT

Currently, additive manufactured titanium alloy Ti-6Al-4V predominantly fails from process-induced defects, when subjected to cyclic loading in the polished condition. These defects not only lead to premature failure, but also contribute to the significant dispersion of fatigue life commonly seen in metal additive manufacturing. In this work, we have studied the source of dispersion and the influence of pore size on fatigue life using samples from the standard processing route and samples with intentionally introduced porosity defects. According to the fracture surface study, contrary to the common belief, the source of dispersion is primarily the pore location, e.g. surface or embedded pore, rather than the pore size. In the case of embedded pores as the failure source, a threshold pore size of approximately 85 μm was observed, below which the wrought level fatigue performance was achieved. For surface pores above the threshold size, fatigue life was reduced by two orders of magnitude, but remained unchanged, even though crack initiating pore size increased roughly by a factor of four. This experimental observation was supported by local elastic stress analysis, which indicated that pores above a certain size could behave like micro-notches suggesting the popular Kitagawa-Takahashi diagrams should be presented with a horizontal asymptote for this alloy.

## 1. Introduction

Process-induced defects in metal additive manufacturing (AM) are the main source of failure under cyclic loading, after the as-built surface roughness is removed. Considering that roughness removal is a routine procedure in industry for safety critical components, fatigue design in presence of defects is one of the primary concerns for the widespread usage of AM, along with other issues such as anisotropic behaviour due to columnar prior β grains [1] and microstructural heterogeneity [1].

Defects in conventional materials reduce fatigue life and cause dispersion in the S-N data. Defects in metal AM behave the same way, a dispersion more than one order of magnitude was observed in [2], and even higher dispersion, along with reduction of fatigue performance compared to defect free condition, was observed in [3]. Reduction of fatigue strength due to defects in AM titanium alloy Ti-6Al-4V varies between 1.5 and 3.0 by looking at the S-N test data [2,4–6], noting that the number of tests were not sufficient to achieve statistically significant results. Difference in the magnitude of fatigue strength reduction is not

only due to the stochastic nature of fatigue but also related to variations in feedstock quality, machine type, process parameters, build direction, and defect population.

There are two types of process-induced defects in metal AM, namely the lack of fusion and porosity. This paper deals with porosity only, which is used interchangeably with the term "defect" in the remainder of this work. Pores are internal, spherical cavities that could originate from entrapped gas between powder particles [7], mishandling of the wires [8], shielding gas during manufacturing [9] or the keyhole mechanism [10,11]. Consequently, many subsets of AM are susceptible to porosity, and pore size is typically less than 100 μm in diameter for AM Ti-6Al-4V.

In the literature, the relationship between defect size and fatigue performance has been investigated mainly at the fatigue strength, a point arbitrarily selected between $10^6$ and $10^7$ cycles. The Kitagawa-Takahashi diagram was used to demonstrate fatigue strength reduction due to defects in [2] then, the El-Haddad modification [12,13] and the Chapetti modification [14] were also shown to capture the defect size influence on fatigue strength. Apparent success of different modification methods and the reported wide range of the El-Haddad

| Nomenclature | | $\sigma_{av\text{-}p}$ | Local elastic stress value that controls fatigue strength in the vicinity of a pore |
|---|---|---|---|
| $\sigma_a$ | Stress amplitude | $\sigma_{av\text{-}c}$ | Local elastic stress value that controls fatigue strength in the vicinity of a crack |
| $\sigma_m$ | Mean stress | $a$ | Crack size |
| $\sigma^{\infty}$ | Applied far-field stress | $A$ | Material parameter |
| $\sigma_{local}$ | Local elastic stress parallel to applied load | $b$ | Basquin exponent |
| $\sigma_f'$ | Fatigue strength coefficient | $d$ | Equivalent pore diameter |
| $\sigma_N$ | Plain specimen fatigue strength at N cycles | $r$ | Ideal spherical pore radius |
| $\sigma_{Np}$ | Reduced fatigue strength at N cycles due to a spherical pore of a certain size | $D_{th}$ | Threshold pore diameter |
| | | $K_t$ | Elastic stress concentration factor |
| $\sigma_{Nc}$ | Reduced fatigue strength at N cycles due to a crack of a certain size | $K_f$ | Fatigue notch factor |
| $\delta$ | Distance to evaluate local elastic stress | $N$ | Cycles to failure |
| $\nu$ | Poisson's ratio | $R$ | Cyclic load ratio |

parameter, by a factor of two, show the empirical nature of this approach. Therefore, it should be arguably used in ad-hoc basis rather than using a fixed value from literature or handbook. Alternatively, in [15] and [16] defect size influence on fatigue strength was investigated by using the equation proposed by Murakami [17]. Mixed success was achieved this way, which could be due to the lack of correlation between the Vickers hardness and fatigue strength for titanium alloys as reported in [18].

Defect size alone is not sufficient to capture complex fatigue behaviour and defect location is an important parameter as well. Experimental programme in [19] showed crack initiating pores were only within 35% of the largest defects, but if defect size and location were considered together, this value was improved to 3%. The importance of defect location also suggests that, the Kitagawa-Takahashi diagrams could be overly conservative for embedded defects, since the diagrams are constructed by considering only the defect size parameter. In the same study, using X-ray computed tomography, it was observed that crack initiation phase corresponded to more than 70% of the total fatigue life. This observation contradicts with the earlier findings in the field, in which cracks were detected after a few hundred cycles owing to presence of defects that leads to an accelerated initiation phase [12,20]. However, this contradicting observation in AM Ti-6Al-4V could be related to limited resolution achieved by using X-ray computed tomography. Nevertheless, from fatigue life prediction perspective, both the crack propagation methods based on fracture mechanics [14,21,22] and the crack initiation methods such as the strain-life [23,24] approach were shown to be successful within the common tolerance bands, suggesting preference from the industry will be more relevant for the method of choice.

In this study, fatigue test specimens were made using the wire + arc additive manufacturing, i.e. WAAM Ti-6Al-4V. Some of the specimens were intentionally introduced with porosity to analyse a wide range of crack initiating pore diameters, which varied roughly by a factor of twenty, a significant improvement over the available literature data. This enabled to interpret fatigue test results from a broader perspective and by using the fractography results, the main source of dispersed fatigue life data and a fatigue design approach were presented in Section 3. Afterwards, in Section 4 suitability of assuming pores as effective cracks was investigated using experimental observations and local elastic stress analysis. Finally, a notch stress approach using nominal stress was presented to predict fatigue life that could be practical for engineering applications.

## 2. Experimental work

Ti-6Al-4V samples used in this study were fabricated via the WAAM processing route. Chemical composition of the feedstock wire and characterization of the microstructure can be found in an earlier work [13]. Two batches of 27 mm thick, 300 mm long bulk material were deposited layer-by-layer following an oscillation scan strategy. Afterwards, deposited bulk material was cut-off from the base plate, then individual blanks were machined and lathe-turned into fatigue samples in cylindrical, hourglass shape. By this way, axis of the samples coincided with the build direction during manufacturing. In one batch, layers corresponding to the gauge section of the fatigue samples were deposited by using intentionally contaminated wires. Prior to manufacturing, these wires were sprayed with the WD-40® organic compound to increase the likelihood of porosity formation during WAAM processing. By using this technique, a change in microstructure and chemical composition was not observed in the earlier studies [8,13] hence, it was assumed as non-intrusive. A total of 23 samples were tested in this condition as opposed to 12 samples from the reference bulk material.

By following the outlined procedure, samples were expected to have low residual stresses prior to testing. Any undesirable build-up of residual stress during manufacturing should be relaxed after the samples were cut-off from the base plate. Furthermore, as measured and calculated in [25], residual stresses are located near the base plate after the manufacturing, which corresponds to the grip section of the samples, i.e. far away from the gauge (test) section.

The next step prior to testing was to remove the machining marks. A sequential grinding procedure by using silicon carbide grinding papers was conducted starting from 600 grit size until 2500 grit size. Finally, the specimen surface was polished using colloidal silica to obtain a scratch-free surface. A representative light microscopy image of the final surface quality can be found in Fig. 1(b). In this figure, two pores are also visible on the surface.

Load-controlled, constant amplitude axial fatigue tests were conducted in air at ambient temperature using a servomotor actuated rig, at a cyclic stress ratio $R = 0.1$ and 10 Hz cyclic loading frequency. The dimensions of the fatigue specimens complied with the recommendations in ASTM E466 standard [26], except for that the transition radius was less than eight times of the diameter as shown in Fig. 1(a). However, all samples had failed from the gauge section despite this nonconformity. The aim was to quantify dispersion in fatigue life associated with defects. In this regard, at least three test repetitions per applied stress level were made to obtain statistically significant data. Fatigue tests were complemented by fracture surface analysis to determine the failure source and measure dimensions of the source, if relevant. To this end, fracture surfaces were cut from the failed samples by using a precision cutter and ultrasonically cleaned around ten minutes subsequently. Afterwards a ZEISS EVO scanning electron microscope (SEM) was used at 20 kV acceleration in secondary electron mode to analyse the fracture surfaces.
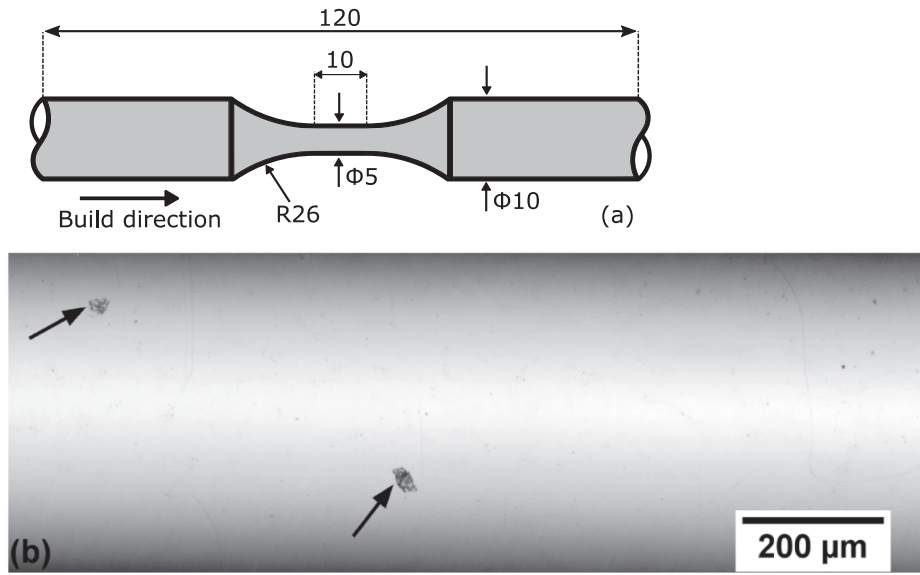
**Fig. 1.** (a) Fatigue specimen geometry and dimensions (mm). Drawing not to scale. (b) Representative image of the surface quality prior to fatigue testing, obtained using light microscopy. Scratch-free surface with initially embedded pores (arrow marking) exposed to the surface after machining to extract hourglass geometry.

## 3. Fatigue test results and dispersion of fatigue life

This section is mainly concerned with dispersion of fatigue life, since most of the engineering codes, such as those documented in [27] and [28], use standard deviation of the test data to determine their design curves. Hence, a high dispersion of fatigue life could make engineering design unfeasible for additively manufactured products, leading to excessively conservative designs, e.g. thicker parts.

Test results are presented in Fig. 2 in the conventional S-N format, including the information about the failure source and crack initiating pore size (microns), if relevant. Individual marker style and size correspond to the crack initiating pore type and diameter, respectively. Calculation of pore diameter is given in Eq. (2) in Section 4. Although failures from clustered pores were marked, their dimensions were not quantified, as the scope of this study was limited to isolated pores. Some of the data points in this diagram were published previously in [13] but in "raw" format, i.e. without the supporting information.

Fig. 2 further corroborates the previous literature findings that surface pores are more detrimental than embedded pores [19,29,30]. The difference in fatigue life could be attributed to lack of microstructure resistance on one side of a surface pore, higher stress triaxiality of an embedded pore or influence of atmospheric conditions. For conventional manufactured Ti-6Al-4V, fatigue crack growth rate is slower in vacuum conditions [31–33], which could be relevant for the embedded keyhole pores in AM. On the other hand, for the embedded gas pores, atmospheric conditions may play a lesser role considering the fatigue crack growth rate in Argon, which is a widely used shielding gas in many AM processes, was found to be similar to the air environment at the low levels of stress intensity factor [34]. A definitive study to determine dominant reason and quantify the reduction rate is an open question according to the authors' best knowledge. It should be added that all process-induced pores were embedded initially, however, during the post-processing stage to achieve desired hourglass geometry and surface finish, embedded pores became exposed to the free surface by the additional material removal. Theoretically, a near-net shape manufacturing with acceptable level of surface finish could result in embedded pores only. Furthermore, in Fig. 2, when attention is concentrated on a single failure source, such as embedded defects, it is
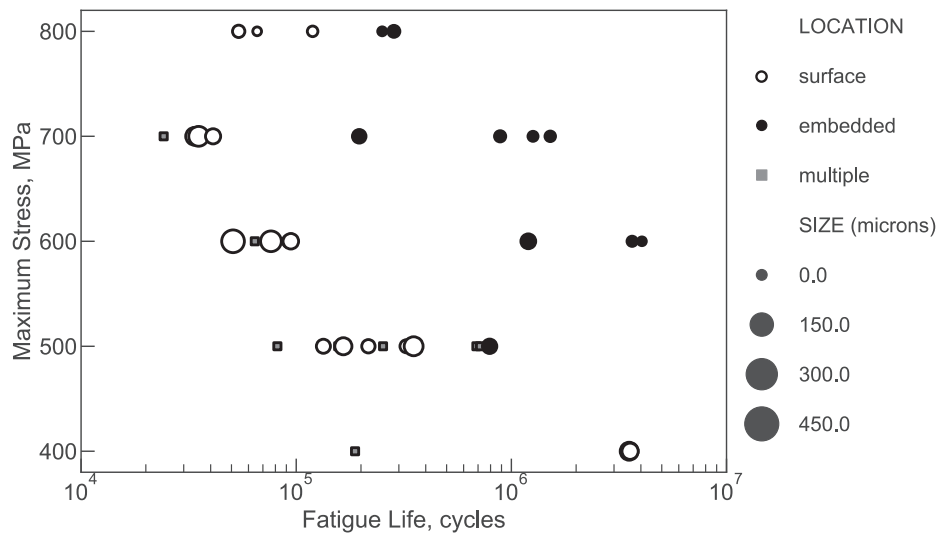


**Fig. 2.** Constant amplitude axial fatigue test results at $R = 0.1$, mirror-polished surface, tested in air and ambient temperature. Data points are scaled to size according to the crack initiating pore diameter (microns) and marked depending on the crack initiating pore location. Eq. (2) was used for calculating the pore size.

observed that larger defects generally result in lower fatigue life. This agrees well with the fracture mechanics understanding, where stress intensity factor increases monotonically with the increase of defect or crack size.

Beyond these general remarks about fatigue behaviour in presence of defects, a dispersion of fatigue life up to two orders of magnitude can be observed in Fig. 2. A literature comparison is challenging at this stage, as most of the previous work did not conduct enough repetitions to reveal fatigue life dispersion or changed an important parameter such as the build direction, making it hard to isolate the effect of defects. Nevertheless, similar dispersion could be observed in [3], but less pronounced dispersion was also reported in [19]. The reason for the latter is attributed to failure from a single source, e.g. surface pores, as found in this work, which will be discussed in the following.

In Fig. 3, fatigue test results at two particular applied stress levels are shown in normal probability plot using the procedure outlined in the standard BS ISO 12107 [35]. At 500 MPa maximum applied stress, where failure occurred mainly due to surface pores, a linear line can be drawn, which confirms the common assumption of normal distribution of fatigue life. However, at 600 MPa applied stress level two distinct groups of fatigue data is visible, suggesting different failure mechanisms could be the main reason of the dispersion. Subsequent fracture surface analysis confirmed this hypothesis. In fact, fractography revealed three different failure sources across the whole experimental programme as shown in Fig. 4.

Three different crack-initiating sources observed in fracture surface analysis are shown in Fig. 4. A surface pore manifested as a semi-circular shape, an embedded pore with a circular morphology and entirely bounded within the bulk material, and a cluster of pores. In this study, only those failures from single pores are considered, i.e. Fig. 4(a) and (b), as the cluster of pores did not occur frequently to analyse further and they were present only in the contaminated batches, hence may not be natural in the WAAM processed Ti-6Al-4V.

### 3.1. Categorising S-N data

This section provides a discussion regarding the source of fatigue life dispersion, presents a way to handle dispersed data and makes connection with a procedure currently used in the welding industry. The latter could be also helpful in metal AM for fatigue design in presence of process-induced defects.

Source of fatigue life dispersion is commonly associated with the variation in crack initiating defect size, e.g. [36]. At first impression, this statement holds true for this work as well. Measurement of crack initiating defect size for the data points shown in Fig. 2 had revealed a range of pore diameters from 20 μm to 400 μm. However, normal probability plot in Fig. 3 suggests two entirely different groups of data, i.e. change of



**Fig. 3.** Normal probability plot; the 600 MPa applied stress level shows two distinct groups of test data suggesting difference in failure source.

failure source, rather than variation of a single parameter. Fracture surface analysis also confirmed that source of failure changed among the test samples. Furthermore, smaller surface pores have shown to be more detrimental than larger embedded pores [19], i.e. no competition among the different failure sources. Considering all these, first highly dispersed data shown in Fig. 2 were labelled according to the failure source that was determined during fractography. Crack initiating pores that showed a semi-circular morphology were labelled as "surface pores", whereas pores with circular morphology were labelled as "embedded pores" and failures due to clustered pores were removed as this study concentrates on isolated porosity only. One exception to this heuristic rule was embedded pores that are less than a diameter away from the surface. These were labelled as "surface pores" as well despite their circular morphology on the fracture surface. Considering the stress concentration factor ($K_t$) calculation using the gross area, the side of the pore that is closer to the surface will inevitably have much higher $K_t$ value due to the reduced loading bearing material between the free surface and the pore. Therefore, it is expected that a crack is formed quickly on this side and it will break to the surface relatively early compared to total fatigue life, acting as a "surface pore" in the remainder. Similar discussion on this subject can be found in the following works as well [12,37,38].

After the labelling, it was possible to fit a linear S-N curve using the least squares regression depending on the failure source, i.e. surface or embedded pores. This calculation is based on Eq. (1) and presented in Table 1 according to the original Basquin relation that was modified by Morrow to accommodate mean stress influence [39]. Furthermore, these failure-type specific S-N curves are given in Fig. 5, in terms of stress amplitude versus stress reversals (2N). Consequently, calculated co-efficients of the Basquin-Morrow equation can be compared with other Ti-6Al-4V fatigue test results available in the literature.

$$\frac{\Delta\sigma}{2} = \sigma_a = \left(\sigma_f' - \sigma_m\right)(2N)^b \tag{1}$$

where $\Delta\sigma$ is the applied stress range, $\sigma_a$ the stress amplitude, $\sigma_m$ the mean stress, $\sigma_f'$ the fatigue strength coefficient and $b$ the Basquin exponent.

A high correlation coefficient, $R^2 \geq 0.9$, was achieved in both S-N curves as shown in Table 1. This suggests that, contrary to common belief, dispersion of S-N data is related to defect type rather than defect size and there is a growing evidence in literature in this direction [40]. Despite the high correlation coefficient, there is markedly larger scatter of results at lower applied stress levels as seen in Fig. 5. This could be attributed to defects, for instance at 500 MPa, crack initiating pore size varied by a factor of 2.5. However, this value is much less compared to 600 MPa applied stress level, where crack initiating pore size varied by a factor of roughly 4.0. Therefore, it is considered that the increased scatter at lower stress levels are associated with the inherent features of fatigue, such as the influence of microstructural heterogeneity that is commonly observed in the high cycle fatigue regime.

From Fig. 5, it can be concluded that a separate S-N curve can be determined for a certain failure type. A similar situation exists in the welding design recommendations, e.g. Hobbacher [41], where according to the weld type or joint configuration, a specific S-N curve exists, the so-called FAT classes. Such a scenario could be suitable for the AM materials, since early literature in AM fatigue has established that there is no competition among the failure sources but rather a clear hierarchy exists [42,43]: Surface roughness in the as-built condition is the most detrimental situation. After eliminating it, process-induced defects, such as porosity, act as main sources of fatigue failure. Finally, if hot isostatic pressing (HIP) is applied as a post treatment, fatigue performance can reach to the wrought material level and fatigue crack initiates from microstructural features. Therefore, for engineering design, a specific S-N curve can be selected depending on the post-processing history.
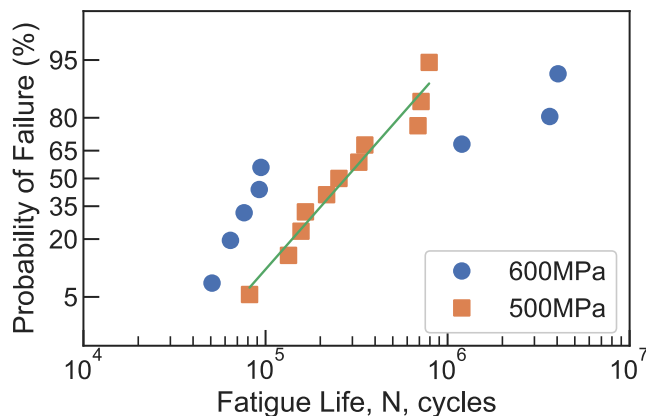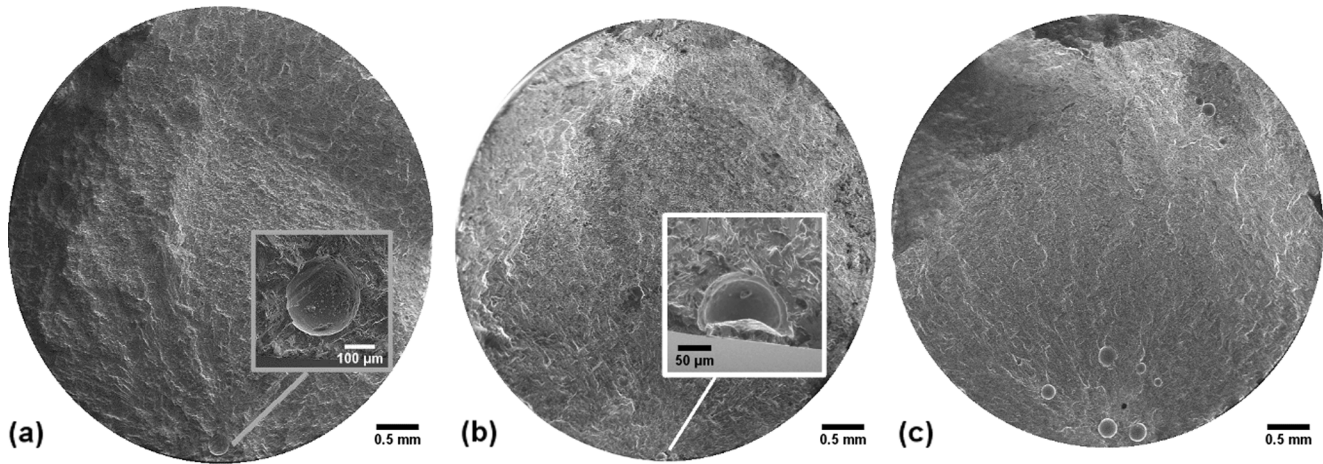
**Fig. 4.** Fracture surface analysis (a) embedded pore, (b) surface pore, (c) clustered pores.

**Table 1**
Results of the least squares regression and material constants in Eq. (1).

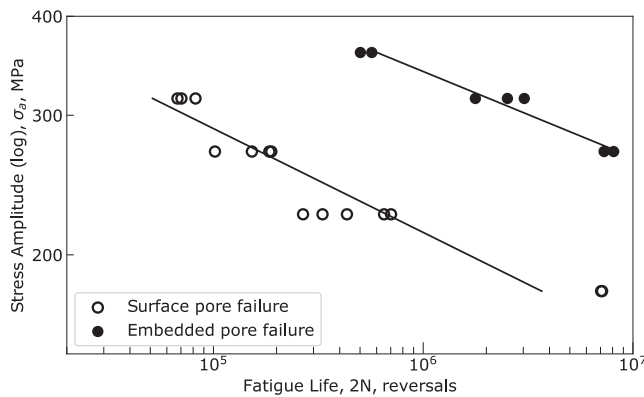|  | Surface pore failure | Embedded pore failure |
|---|---|---|
| $\sigma_f' - \sigma_m$ (MPa) | 1305 | 1527 |
| $b$ | −0.131 | −0.109 |
| No. of data points | 14 | 7 |
| Correlation Coefficient ($R^2$) | 0.896 | 0.962 |



**Fig. 5.** Individual S-N curves based on the failure source. Similar plots can be seen in the welding industry design codes where engineers use individual S-N curves depending on joint type.

## 4. Influence of pore size on fatigue life

In the literature, the effect of defect size on fatigue performance is commonly investigated using the Kitagawa-Takahashi (K-T) diagram or certain modifications of it. The K-T diagram can be classified as a constant life plot, in which fatigue strength is plotted against crack initiating defect size. For this study, instead of determining a fatigue strength value at an arbitrary number of cycles, a constant stress approach was attempted. As a result, plots analogous to K-T diagram were produced by repeating fatigue tests at the selected stress levels, assuming that fatigue life at a given stress value is a random variable with a certain statistical distribution. Hence, when fatigue life is used instead of fatigue strength, influence of defects can be seen, in terms of a deviation from the sample mean value of fatigue life. Experimental results analysed in this manner are plotted in Fig. 6(a) and (b), which corresponds to the maximum applied stress values of 700 MPa and 600 MPa, respectively. To put these results into context, fatigue life of a wrought Ti-6Al-4V was taken from page 553 of material properties handbook [44] and marked in these

figures.

Pore diameters in Fig. 6 were measured directly from the fracture surface obtained from the SEM images. First, a spline was fitted along the crack-initiating pore to establish boundaries, and then area inside this boundary was calculated by using the open-source image analysis software ImageJ [45], which counts the number of pixels to quantify this value. Afterwards, equivalent pore diameter was calculated using Eq. (2):

$$d = 2\sqrt{\frac{\text{Area}}{\pi}} \tag{2}$$

Based on the experimental data, a threshold pore diameter, $D_{\text{th}}$, roughly around 85 μm can be estimated, which is marked by a dashed red line in Fig. 6. Below this threshold diameter, wrought level performance was achieved by the WAAM process, despite the presence of defects. At this point, it is important to underscore the potential difference in failure sources between the wrought and AM material. Although the failure source of the wrought data was not provided in the referenced handbook [44], it would be fair to assume a microstructure related failure, e.g. surface initiation due to an unfavourably oriented grain, which is typical for high-cycle fatigue regime ($N \leq 10^7$ cycles) of smooth-surface fatigue test coupons. This suggests that AM material had reached the wrought fatigue performance despite the embedded pores as the failure source, therefore in the absence of defects, AM material might perform even better compared to its wrought counterpart. The reason could be traced back to the metallurgy of titanium alloys, where fine microstructure, as commonly seen in AM, is shown to have better high-cycle fatigue performance compared to coarser microstructures owing to reduced effective slip length [46, pg. 217]. Having said that, wrought fatigue data extracted from the handbook is at least 30 years old at this stage and more recent test data would provide a better picture.

Above 85 μm diameter, a significant drop in fatigue life can be observed, between an order of magnitude one to two. The degree of fatigue life reduction was found to be different for embedded and surface pores. However, not enough embedded pores were observed in current tests to quantify this difference in a statistically significant way. Furthermore, the threshold diameter of 85 μm was observed based on the embedded pores considering that surface pores are more detrimental as seen in Fig. 6 and discussed in Section 3, the threshold diameter for surface pores could be smaller. For instance, Hu et al. [14] suggests 11 μm threshold diameter, albeit for a different AM process. A change in threshold pore diameter due to defect location was undetected, since smaller surface pores were not present among the fatigue samples tested in this experimental programme.

Secondly, above the threshold pore diameter, although fatigue life was reduced due to porosity, it was insensitive to changes in pore size. In
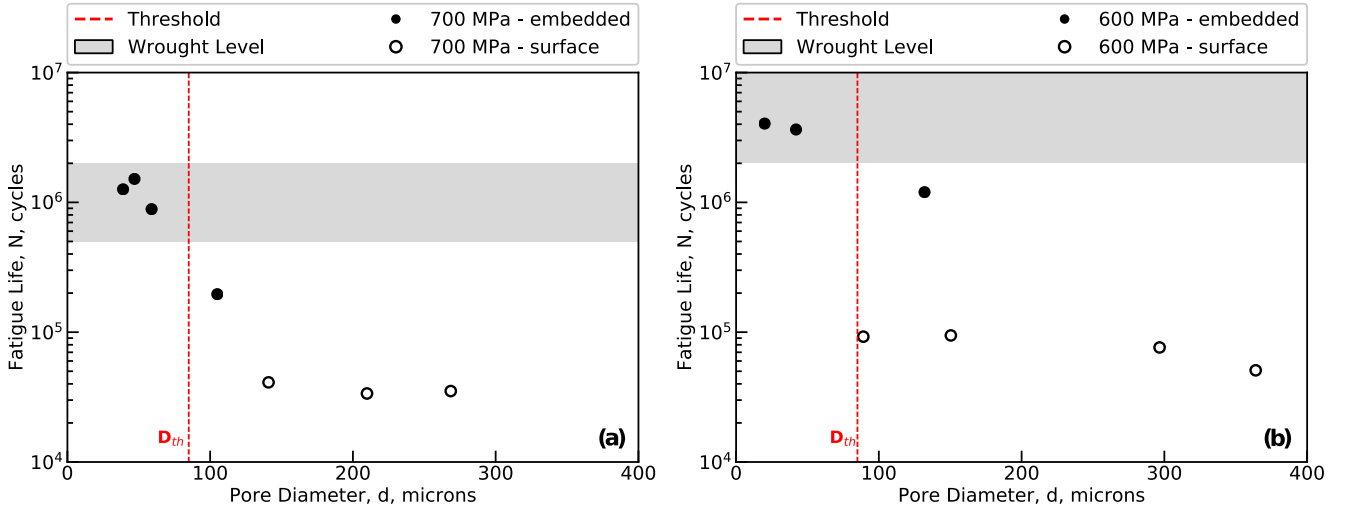
**Fig. 6.** Influence of pore size on fatigue life at given maximum applied stress. (a) 700 MPa, (b) 600 MPa, wrought fatigue data is from [44]

fact, at applied stress level 600 MPa, even though the crack initiating pore diameter increased roughly by four times, fatigue life stayed almost constant. The reason behind this behaviour is linked to the pore morphology in the following subsection hence even the though the observation was made only for surface pores, we have no reason to suspect its validity for the embedded pores.

### 4.1. Pores and small cracks: the difference

This section deals with pores larger than the threshold size, which was found to be around 85 μm for this particular manufacturing batch. The aim is to scrutinize the experimental observations shown in Fig. 6 and provide a discussion about the suitability of assuming pores as small cracks, which is a common approach in engineering analysis to evaluate criticality of defects [36].

Fig. 6 is a constant stress diagram that shows the change in fatigue life according to the crack initiating pore size. Because of working with natural defects, crack initiating pore diameter varied from 20 μm to 400 μm, making it impractical to choose an appropriate stress level to reach constant fatigue life, such as $10^7$ cycles in the conventional K-T diagrams that show the change in fatigue strength according to the defect size. Nevertheless, fatigue strength of a defect-free material at a particular fatigue life *N*, $\sigma_N$, will reduce due to porosity and this reduction should roughly follow the trend of fatigue life behaviour observed in Fig. 6, albeit at a different scale, considering the classical power-law

relationship in Eq. (1) between applied stress and fatigue life. In other words, reduction in fatigue strength should reach to a constant value like the fatigue life beyond the threshold pore size as seen in Fig. 6.

In presence of stress raisers, such as pores or small cracks, it is commonly assumed that fatigue life is not directly related to the peak elastic stress but rather controlled by an averaged local stress value. A convenient way to calculate this average stress is using the local stress value at a certain distance away from the peak stress, i.e. the so-called point method [47], which is sketched in Fig. 7. The physical meaning of this distance is not discussed further, since it was merely seen as a fitting parameter.

As briefly explained in the introduction, pores in AM usually stem from remaining gas bubbles after processing, hence they can be approximated as spheres. This morphology of pores can be observed from the fracture surface analysis in Fig. 4 and is confirmed by X-ray computer tomography measurements in [7,19,48]. Local elastic stress distribution near a spherical cavity in an infinite body has a closed-form solution, which was given by the Goodier-Timoshenko elasticity solution [49] in Eq. (3).

$$\sigma_{local}(x) = \sigma^{\infty}\left[1.0 + \frac{4 - 5\vartheta}{14 - 10\vartheta}\left(\frac{r^3}{(x+r)^3}\right) + \frac{9}{14 - 10\vartheta}\left(\frac{r^5}{(x+r)^5}\right)\right] \quad (3)$$

where $\sigma_{local}$ is the local stress component parallel to the load direction, $\sigma^{\infty}$ the far-field applied stress, $\nu$ the Poisson's ratio, *x* the distance from pore edge perpendicular to the loading direction and *r* the pore radius.
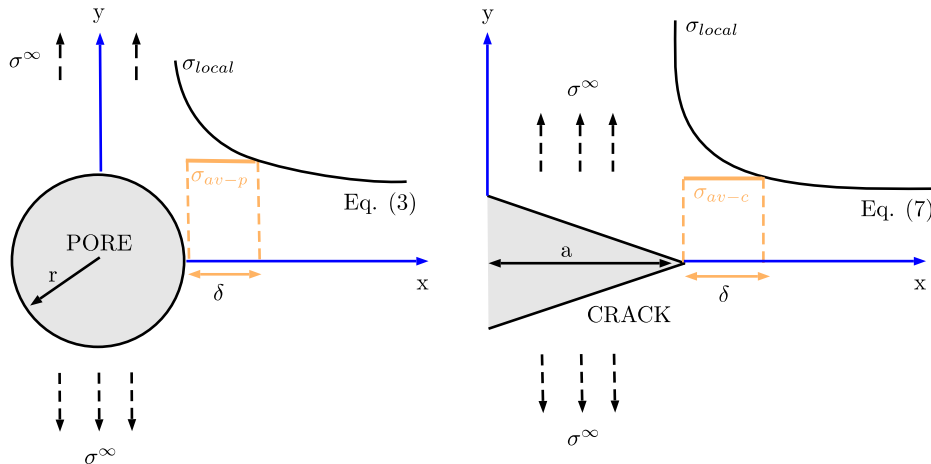


**Fig. 7.** Sketches of local elastic stress distribution around a pore and a crack under far-field tensile loading along the y-direction.

Note that by adopting elasticity formulation, it is inherently assumed that pore is sufficiently larger than the grain size, so that homogenous material axiom is valid, yet pore is small enough, so that $K_t$ stays constant with changing diameter, i.e. infinite body clause.

Considering a defect-free sample with fatigue strength $\sigma_N$ at a particular fatigue life $N$, reduced fatigue strength due to a pore, $\sigma_{Np}$, using the local stress approach can be calculated as follows:

$$\sigma_{local}(\delta) = \sigma_{av-p} = \sigma_N \left[ 1.0 + \frac{4-5\vartheta}{14-10\vartheta} \left( \frac{r^3}{(\delta+r)^3} \right) + \frac{9}{14-10\vartheta} \left( \frac{r^5}{(\delta+r)^5} \right) \right]$$

(4)

$$\sigma_{Np} = \frac{\sigma_N}{K_f} \text{ where } K_f = \frac{\sigma_{av-p}}{\sigma_N}$$

(5)

$$\text{when } r \gg \delta \rightarrow \frac{\sigma_{Np}}{\sigma_N} = \left( \frac{27-15\vartheta}{14-10\vartheta} \right)^{-1} = \text{constant}$$

(6)

Although cracks are traditionally analysed using fracture mechanics, the concept of controlling local stress can be extended to analyse cracks as shown by Taylor [50]. Local elastic stress in the vicinity of a crack can be calculated according to Westergaard as follows:

$$\sigma_{local}(x) = \frac{\sigma^\infty}{\sqrt{\left[ 1 - \left( \frac{a}{x+a} \right)^2 \right]}}$$

(7)

where $\sigma_{local}$ is the local elastic stress component parallel to the load direction, $\sigma^\infty$ the far-field applied stress, $x$ the distance from crack tip perpendicular to the loading direction and $a$ the crack size. Alternatively, for long cracks, this equation can be expressed as:

$$\sigma_{local}(x) = \frac{\sigma^\infty \sqrt{\pi a}}{\sqrt{2\pi x}} = \sigma^\infty \sqrt{a/2x}$$

(8)

In presence of a crack, reduced fatigue strength, $\sigma_{Nc}$, compared to the crack-free condition, $\sigma_N$, can be calculated similarly by following the steps in Eqs. (4) to (6):

$$\text{when } a \gg \delta \rightarrow \frac{\sigma_{Nc}}{\sigma_N} = \frac{1}{\sqrt{a/2\delta}}$$

(9)

By comparing Eqs. (6) and (9), influence of spherical, i.e. blunt, morphology of pores becomes apparent. When pore size, $r$, is sufficiently larger than the distance, $\delta$, where local average stress is evaluated, Eq. (4) reduces to a constant value that depends on the Poisson's ratio only as shown in Eq. (6). In other words, it becomes independent of the pore size as observed in the experiments. On the other hand, as the crack size, $a$, increases, according to Eq. (9), fatigue strength value will decrease monotonically. This difference of behaviour is further illustrated in Fig. 8.

In order to reach the horizontal asymptote in Fig. 8 at the threshold pore diameter of ~85 μm seen in the experiments, evaluation distance, $\delta$, is found to be less than 10 μm. This suggests that, for pores larger than the threshold size, fatigue notch factor is roughly equal to the stress concentration factor, i.e. full notch sensitivity for this particular alloy. Using such a small $\delta$ value, experimental results are re-plotted side-by-side with the calculated the trend of fatigue strength reduction in Fig. 9.

The difference between treating a pore as a crack and a notch can be observed from Fig. 9. Crack behaviour using the local stress concept follows the well-established Kitagawa-Takahashi type trend, which fails to capture pore behaviour beyond the threshold size observed in experiments (Fig. 6). On the other hand, by treating the pores as notches, a roughly constant fatigue life, i.e. horizontal asymptote, can be obtained as seen in the experiments despite the increasing crack initiating pore size.

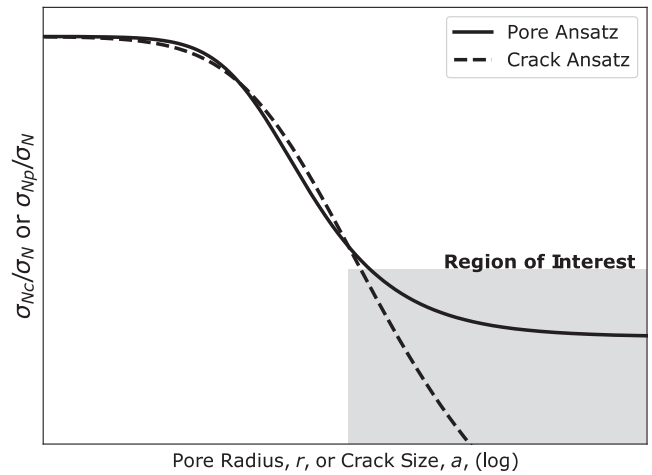To summarize, when evaluating criticality of a pore, considering it as



**Fig. 8.** Reduction of fatigue strength ($\sigma_N$) at a particular fatigue life N; it differs after a certain size depending on the notch assumption ($\sigma_{Np}$, Eq. (6)) and crack assumption ($\sigma_{Nc}$, Eq. (9)).

a small crack could lead to overly conservative estimations in some cases. In practice, this is especially important for fine grain materials, where the critical distance, $\delta$, is small. Therefore, notch behaviour could be observed even for small micron-sized pores as in this work. Further evidence can be found in literature of high strength alloys, for instance [52] reported a notch behaviour as well for small holes larger than 100 μm in diameter. This finding forms the basis for fatigue life prediction in the following section.

## 5. Notch fatigue approach for S-N curve prediction

In practice, fracture mechanics approach is often preferred to analyse fatigue life in presence of defects, e.g. [53]. The rationale behind this preference is based on the observational evidence of cracks initiating early from defects [20,36]. Furthermore, fracture mechanics makes it is possible to consider the pore size influence using the stress intensity factor, whereas the stress concentration factor for a spherical pore in a large body is independent of the pore size as it can be deduced by the local elastic stress distribution given in Eq. (3) by setting the $x$ value to zero. However, as shown in the previous section using the theory of critical distances [47], even micron-sized pores can behave like notches if the critical distance is small, which is common in high-strength materials as used in this work. Such a notch behaviour was observed in the experiments for surface pores larger than 85 μm as seen in Fig. 6. Therefore, in this section, the notch stress approach is presented as an alternative way to analyse fatigue life in presence of defects for WAAM Ti-6Al-4V.

As mentioned in the introduction and Section 4.1, pores originate from shielding gas bubbles that are entrapped in the melt pool and therefore can be approximated as spheres. Elastic stress concentration factor of a spherical cavity in an infinite body has a closed-form solution, which is given in Eq. (10). This equation can be found in handbooks such as [54] and obtained by using the Eshelby inclusion method [55] or Timoshenko elasticity solution [49].

$$K_t = \frac{27-15\vartheta}{14-10\vartheta}$$

(10)

For Ti-6Al-4V, Poisson's ratio ($\nu$) is 0.34, which yields a stress concentration factor $K_t$ roughly around two. It should be noted that similar to a hole in an infinite plate, where $K_t$ is constant and equal to three independent of hole size, this equation is also valid regardless of the pore diameter.

Elastic stress concentration factor $K_t$ was taken equal to the fatigue notch factor $K_f$, as discussed in the previous section. Another way to
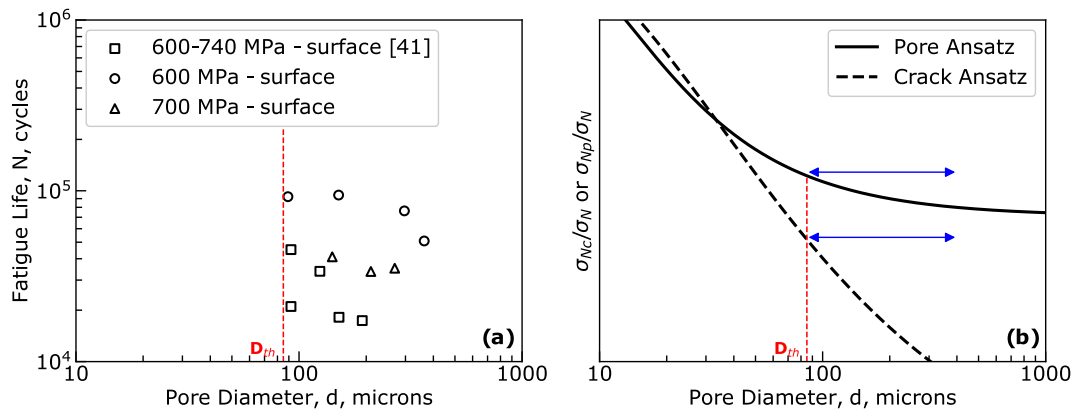
**Fig. 9.** (a) Experimental results beyond the threshold pore size re-plotted from Fig. 6 along with results from [51]. Fatigue life almost stays constant even though crack initiating pore size increases. (b) Range of crack initiating pores is marked with double-headed arrows. Notch assumption of pores follows the experimental trend; reduction from defect-free nominal fatigue strength saturates to a horizontal asymptote, whereas the crack assumption leads to monotonically decreasing trend.

think about this assumption is the higher notch sensitivity exhibited by high-strength or fine-grain materials. This can be observed using the empirical equations to estimate fatigue notch factor, for instance by Neuber in page 178 of [56], as given in Eq. (11).

$$\frac{K_f}{K_t} = \frac{1 + \frac{1}{K_t}\sqrt{A/d}}{1 + \sqrt{A/d}} \tag{11}$$

In Eq. (11), $A$ is the material parameter that is associated with the controlling microstructural feature, which is assumed as the grain size, and $d$ is the pore diameter. This equation is plotted for various sizes of pore and material parameters using $K_t = 2.08$ in Fig. 10.

Empirical nature of Eq. (11) means that absolute values would not be applicable, but the main trend from Fig. 10 is clear: material parameter is more dominant than the size effect of a notch and the ratio $K_f/K_t$ approaches to unity, as the grain size gets finer. Fine grain size is an inherent feature of the AM, since during processing, a micron layer of material is melted and re-melted repeatedly, leading to a high cooling rates. According to page 219–221 of Lütjering and Williams [46], for titanium alloys without the alpha colony microstructure, controlling fatigue parameter is the thickness of individual alpha laths, which is about 1–2 µm for WAAM Ti-6Al-4V [13]. As a result, in this work full notch sensitivity was assumed, i.e. $K_f = K_t$.

Next, in order to generate S-N curve for surface pores, the defect-free fatigue strength at $10^7$ cycles given in [13] was divided by fatigue notch factor $K_f$ to generate the first point at $10^7$ cycles in Fig. 11. The second point was drawn according to a textbook approach, see for instance page 206 of [56], where fatigue life at $10^3$ cycles is equal to the ultimate
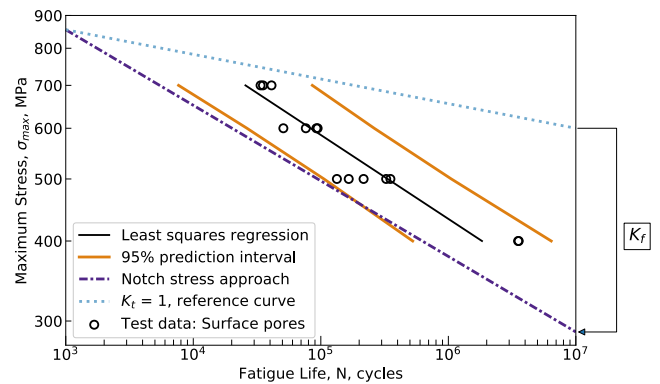


**Fig. 10.** Relationship of fatigue notch factor ($K_f$) with the material parameter ($A$) for three representative pore diameters ($d$).



**Fig. 11.** Fatigue life prediction for surface pores using the notch stress approach.

tensile strength. The resulting prediction curve is given in Fig. 11, together with the test data. Tolerance bands on the test data in this figure were calculated using the Welding Institute guideline for statistical analysis of fatigue data [57]. This guideline assumes a common lognormal distribution of fatigue life data at a given stress level, and then uses the Students $t$-distribution to calculate tolerance bands.

As shown in Fig. 11, the notch stress approach was found to be conservative when compared to the mean fatigue test results, yet it lies within the 95% prediction interval of the experimental data. The authors have refrained from using additional data points from the literature, as failure source is often omitted. Furthermore, at the current state of technology, batch-to-batch variation could lead to significant differences depending on wire quality, selected process parameters etc. This problem can be observed from the recent review papers, such as [42], where S-N data collected from literature is presented in a single plot. Therefore, in the authors' view, defect-free fatigue strength should ideally be determined every time when the process parameters or feedstock material is changed. Although this would not influence the presented approach, numerical results will change depending on the manufacturing quality, i.e. the S-N curves might shift upwards or downwards accordingly. As the manufacturing technology matures, it is expected that a "default" S-N curve for AM material could be established.

Finally, the aim of this section was to show feasibility of the notch stress approach for evaluating pores in AM. In order to focus on influence of porosity, this paper had dealt with $R = 0.1$ loading only; when extrapolating presented results to a different stress ratio, one should
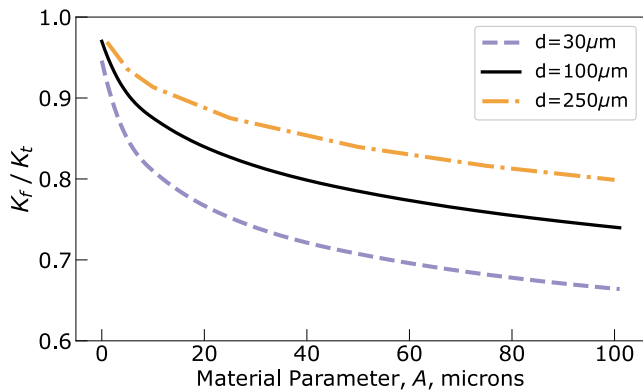
exercise caution as the mean stress was shown to influence fatigue notch factor $K_f$ significantly [58]. Compared to the strain-life approaches [23,24], the elastic notch stress approach provides a practical way to assess structural integrity. This is because explicit modelling of the pore is not necessary and it can be constructed by using load-controlled fatigue tests as opposed to cyclic stress–strain data, which is not widely available at the moment. Prediction quality of the presented approach can be further improved, e.g. by measuring the fatigue strength at 1000 cycles, instead of assuming it equal to the tensile strength. Furthermore, for surface pores, stress concentration factor ($K_t$) will differ depending on the depth of the defect embedded inside the material. This variation in $K_t$ was not considered in this work and it could potentially lead to improved accuracy in fatigue life prediction.

## 6. Conclusions

In this work, fatigue behaviour of wire + arc additive manufactured titanium alloy Ti-6Al-4V in polished condition was investigated under constant amplitude axial loading in air at ambient temperature. Cylindrical hourglass test coupons were extracted from manufactured blanks and some of these coupons were subjected to a non-intrusive way of introducing porosity, which enabled studying a wide range of crack initiating pore diameters. The following conclusions can be drawn:

- Consistent with the literature, in polished condition, additively manufactured fatigue samples failed predominantly due to process-induced defects. Fracture surface analysis revealed three different crack initiation sources: surface pore, embedded pore and multiple pores clustered together. Although all defects were embedded in the as-built condition, subsequent material removal to achieve hourglass sample geometry resulted in formation of surface pores. Multiple pores were mainly seen in the intentionally contaminated batches; hence, they might be preventable, if best-practice measures are taken during manufacturing.
- Commonly seen dispersion in S-N data of AM metals were found to be associated with the defect location, such as surface pore or embedded pore, rather than the pore size for this particular alloy. Consequently, for engineering design, individual S-N curves are suggested according to the defect type. A similar approach is already implemented in the welding industry based on the joint type.
- Pores larger than the 85 µm diameter reduced fatigue life, but they did not act as cracks obeying the Kitagawa-Takahashi diagram, which is a common assumption in the field. When process-induced pores, although in micron scale, were treated as notches, their behaviour matched with the experimental observations. Notch behaviour observed in micron scale was linked to the pore morphology and the extremely fine microstructure seen in metal additive manufacturing due to the repeated melting and rapid cooling of thin layers of the feedstock material.
- The notch stress approach was shown to predict surface pore S-N curve within 95% of the prediction interval.

## Declaration of Competing Interest

The authors declare that they have no known competing financial interests or personal relationships that could have appeared to influence the work reported in this paper.

## Acknowledgements

## References

[1] Seifi M, Salem A, Satko D, Shaffer J, Lewandowski JJ. Defect distribution and microstructure heterogeneity effects on fracture resistance and fatigue behavior of EBM Ti–6Al–4V. Int J Fatigue 2017;94:263–87. https://doi.org/10.1016/j.ijfatigue.2016.06.001.

[2] Wycisk E, Solbach A, Siddique S, Herzog D, Walther F, Emmelmann C. Effects of Defects in Laser Additive Manufactured Ti-6Al-4V on Fatigue Properties. Phys Procedia 2014;56:371–8. https://doi.org/10.1016/j.phpro.2014.08.120.

[3] Greitemeier D, Palm F, Syassen F, Melz T. Fatigue performance of additive manufactured TiAl6V4 using electron and laser beam melting. Int J Fatigue 2017;94:211–7. https://doi.org/10.1016/j.ijfatigue.2016.05.001.

[4] Zhao Xiaoli, Li Shujun, Zhang Man, Liu Yandong, Sercombe Timothy B, Wang Shaogang, et al. Comparison of the microstructures and mechanical properties of Ti–6Al–4V fabricated by selective laser melting and electron beam melting. Mater Des 2016;95:21–31. https://doi.org/10.1016/j.matdes.2015.12.135.

[5] Chastand V, Quaegebeur P, Maia W, Charkaluk E. Comparative study of fatigue properties of Ti-6Al-4V specimens built by electron beam melting (EBM) and selective laser melting (SLM). Mater Charact 2018;143:76–81. https://doi.org/10.1016/j.matchar.2018.03.028.

[6] Hrabe N, Gnäupel-Herold T, Quinn T. Fatigue properties of a titanium alloy (Ti–6Al–4V) fabricated via electron beam melting (EBM): Effects of internal defects and residual stress. Int J Fatigue 2017;94:202–10. https://doi.org/10.1016/j.ijfatigue.2016.04.022.

[7] Cunningham Ross, Nicolas Andrea, Madsen John, Fodran Eric, Anagnostou Elias, Sangid Michael D, et al. Analyzing the effects of powder and post-processing on porosity and properties of electron beam melted Ti-6Al-4V. Mater Res Lett 2017;5(7):516–25. https://doi.org/10.1080/21663831.2017.1340911.

[8] Wang Fude, Williams Stewart, Colegrove Paul, Antonysamy Alphons A. Microstructure and Mechanical Properties of Wire and Arc Additive Manufactured Ti-6Al-4V. Metall Mater Trans A 2013;44(2):968–77. https://doi.org/10.1007/s11661-012-1444-6.

[9] DebRoy T, Wei HL, Zuback JS, Mukherjee T, Elmer JW, Milewski JO, et al. Additive manufacturing of metallic components – Process, structure and properties. Prog Mater Sci 2018;92:112–224. https://doi.org/10.1016/j.pmatsci.2017.10.001.

[10] King Wayne E, Barth Holly D, Castillo Victor M, Gallegos Gilbert F, Gibbs John W, Hahn Douglas E, et al. Observation of keyhole-mode laser melting in laser powder-bed fusion additive manufacturing. J Mater Process Technol 2014;214(12):2915–25. https://doi.org/10.1016/j.jmatprotec.2014.06.005.

[11] Zhao Cang, Fezzaa Kamel, Cunningham Ross W, Wen Haidan, De Carlo Francesco, Chen Lianyi, et al. Real-time monitoring of laser powder bed fusion process using high-speed X-ray imaging and diffraction. Sci Rep 2017;7(1). https://doi.org/10.1038/s41598-017-03761-2.

[12] Beretta S, Romano S. A comparison of fatigue strength sensitivity to defects for materials manufactured by AM or traditional processes. Int J Fatigue 2017;94:178–91. https://doi.org/10.1016/j.ijfatigue.2016.06.020.

[13] Biswal R, Zhang X, Syed AK, Awd M, Ding J, Walther F, et al. Criticality of porosity defects on the fatigue performance of wire + arc additive manufactured titanium alloy. Int J Fatigue 2019;122:208–17. https://doi.org/10.1016/j.ijfatigue.2019.01.017.

[14] Hu YN, Wu SC, Wu ZK, Zhong XL, Ahmed S, Karabal S, et al. A new approach to correlate the defect population with the fatigue life of selective laser melted Ti-6Al-4V alloy. Int J Fatigue 2020;136:105584. https://doi.org/10.1016/j.ijfatigue.2020.105584.

[15] Leuders Stefan, Vollmer Malte, Brenne Florian, Tröster Thomas, Niendorf Thomas. Fatigue Strength Prediction for Titanium Alloy TiAl6V4 Manufactured by Selective Laser Melting. Metall Mater Trans A 2015;46(9):3816–23. https://doi.org/10.1007/s11661-015-2864-x.

[16] Benedetti M, Fontanari V, Bandini M, Zanini F, Carmignato S. Low- and high-cycle fatigue resistance of Ti-6Al-4V ELI additively manufactured via selective laser melting: Mean stress and defect sensitivity. Int J Fatigue 2018;107:96–109. https://doi.org/10.1016/j.ijfatigue.2017.10.021.

[17] Murakami Y. Material defects as the basis of fatigue design. Int J Fatigue 2012;41:2–10. https://doi.org/10.1016/j.ijfatigue.2011.12.001.

[18] Murakami Y. 13 - Ti alloys. In: Murakami Y, editor. Met. Fatigue Second Ed. 2nd ed., Academic Press 2019, p. 293–316. https://doi.org/10.1016/B978-0-12-813876-2.00013-3.

[19] Tammas-Williams S, Withers PJ, Todd I, Prangnell PB. The Influence of Porosity on Fatigue Crack Initiation in Additively Manufactured Titanium Components. Sci Rep 2017;7:7308. https://doi.org/10.1038/s41598-017-06504-5.

[20] MURAKAMI Y, ENDO M. Effects of defects, inclusions and inhomogeneities on fatigue strength. Int J Fatigue 1994;16(3):163–82. https://doi.org/10.1016/0142-1123(94)90001-9.

[21] Jones R, Raman RKS, Iliopoulos AP, Michopoulos JG, Phan N, Peng D. Additively manufactured Ti-6Al-4V replacement parts for military aircraft. Int J Fatigue 2019; 124:227–35. https://doi.org/10.1016/j.ijfatigue.2019.02.041.

[22] Yates John R, Efthymiadis Panos, Antonysamy Alphons A, Pinna Christophe, Tong Jie. Do additive manufactured parts deserve better? Fatigue Fract Eng Mater Struct 2019;42(9):2146–54. https://doi.org/10.1111/ffe.v42.910.1111/ffe.13092.

[23] Biswal R, Syed AK, Zhang X. Assessment of the effect of isolated porosity defects on the fatigue performance of additive manufactured titanium alloy. Addit Manuf 2018;23:433–42. https://doi.org/10.1016/j.addma.2018.08.024.

[24] Dinh TD, Vanwalleghem J, Xiang H, Erdelyi H, Craeghs T, Paepegem W Van. A unified approach to model the effect of porosity and high surface roughness on the fatigue properties of additively manufactured Ti6Al4V alloys. Addit Manuf 2020;33:101139. https://doi.org/10.1016/j.addma.2020.101139.

[25] Ahmad Bilal, van der Veen Sjoerd O, Fitzpatrick Michael E, Guo Hua. Measurement and modelling of residual stress in wire-feed additively manufactured titanium. Mater Sci Technol 2018;34(18):2250–9. https://doi.org/10.1080/02670836.2018.1528747.

[26] E08 Committee. E466: Practice for Conducting Force Controlled Constant Amplitude Axial Fatigue Tests of Metallic Materials. ASTM International n.d. https://doi.org/10.1520/E0466-15.

[27] American Society of Mechanical Engineers, Boiler and Pressure Vessel Committee, American Society of Mechanical Engineers. 2019 ASME boiler and pressure vessel code: an international code [Section VIII]. New York: Am Soc Mech Eng 2019.

[28] Rennert R, Forschungskuratorium Maschinenbau, editors. Analytical strength assessment of components: made of steel, cast iron and aluminum materials in mechanical engineering FKM Guideline. 6th, rev. ed ed. Frankfurt Am Main: VDMA-Verl 2013.

[29] Masuo Hiroshige, Tanaka Yuzo, Morokoshi Shotaro, Yagura Hajime, Uchida Tetsuya, Yamamoto Yasuhiro, et al. Influence of defects, surface roughness and HIP on the fatigue strength of Ti-6Al-4V manufactured by additive manufacturing. Int J Fatigue 2018;117:163–79. https://doi.org/10.1016/j.ijfatigue.2018.07.020.

[30] Sterling AJ, Torries B, Shamsaei N, Thompson SM, Seely DW. Fatigue behavior and failure mechanisms of direct laser deposited Ti–6Al–4V. Mater Sci Eng A 2016;655: 100–12. https://doi.org/10.1016/j.msea.2015.12.026.

[31] Oguma H, Nakamura T. Fatigue crack propagation properties of Ti–6Al–4V in vacuum environments. Int J Fatigue 2013;50:89–93. https://doi.org/10.1016/j.ijfatigue.2012.02.012.

[32] Yoshinaka F, Nakamura T, Nakayama S, Shiozawa D, Nakai Y, Uesugi K. Non-destructive observation of internal fatigue crack growth in Ti–6Al–4V by using synchrotron radiation μCT imaging. Int J Fatigue 2016;93:397–405. https://doi.org/10.1016/j.ijfatigue.2016.05.028.

[33] Junet Arnaud, Messager Alexandre, Boulnat Xavier, Weck Arnaud, Boller Elodie, Helfen Lukas, et al. Fabrication of artificial defects to study internal fatigue crack propagation in metals. Scr Mater 2019;171:87–91. https://doi.org/10.1016/j.scriptamat.2019.05.018.

[34] Yoshinaka F, Nakamura T, Takaku K. Effects of vacuum environment on small fatigue crack propagation in Ti–6Al–4V. Int J Fatigue 2016;91:29–38. https://doi.org/10.1016/j.ijfatigue.2016.05.024.

[35] International Organization for Standardization. ISO 12107: Metallic materials — Fatigue testing — Statistical planning and analysis of data. ISO 2003.

[36] Zerbst U, Madia M, Klinger C, Bettge D, Murakami Y. Defects as a root cause of fatigue failure of metallic components. I: Basic aspects. Eng Fail Anal 2019;97: 777–92. https://doi.org/10.1016/j.engfailanal.2019.01.055.

[37] Pineau A, Antolovich SD. Probabilistic approaches to fatigue with special emphasis on initiation from inclusions. Int J Fatigue 2016;93:422–34. https://doi.org/10.1016/j.ijfatigue.2016.09.002.

[38] Rotella Antonio, Nadot Yves, Piellard Mickaël, Augustin Rémi, Fleuriot Michel. Influence of defect morphology and position on the fatigue limit of cast Al alloy: 3D characterization by X-ray microtomography of natural and artificial defects. Mater Sci Eng A 2020;785:139347. https://doi.org/10.1016/j.msea.2020.139347.

[39] Suresh S. Fatigue of Materials. 2nd ed. Cambridge University Press 1998. https://doi.org/10.1017/CBO9780511806575.

[40] Le Viet-Duc, Pessard Etienne, Morel Franck, Prigent Serge. Fatigue behaviour of additively manufactured Ti-6Al-4V alloy: The role of defects on scatter and statistical size effect. Int J Fatigue 2020;140:105811. https://doi.org/10.1016/j.ijfatigue.2020.105811.

[41] Hobbacher A, International Institute of Welding, editors. Recommendations for fatigue design of welded joints and components: IIW document IIW-2249-15, ex XIII-2460-13/XV-1440-13. 2nd ed. Cham Heidelberg New York: Springer 2016.

[42] Li P, Warner DH, Fatemi A, Phan N. Critical assessment of the fatigue performance of additively manufactured Ti–6Al–4V and perspective for future research. Int J Fatigue 2016;85:130–43. https://doi.org/10.1016/j.ijfatigue.2015.12.003.

[43] Cao Fei, Zhang Tiantian, Ryder Matthew A, Lados Diana A. A Review of the Fatigue Properties of Additively Manufactured Ti-6Al-4V. JOM 2018;70(3):349–57. https://doi.org/10.1007/s11837-017-2728-5.

[44] Welsch G, Boyer R, Collings EW, editors. Materials properties handbook: titanium alloys. ASM International: Materials Park, OH; 1994.

[45] Schneider Caroline A, Rasband Wayne S, Eliceiri Kevin W. NIH Image to ImageJ: 25 years of image analysis. Nat Methods 2012;9(7):671–5. https://doi.org/10.1038/nmeth.2089.

[46] Lütjering G, Williams JC. Titanium. 2nd ed. Berlin New York: Springer; 2007.

[47] Taylor D. The theory of critical distances: a new perspective in fracture mechanics. Amsterdam London: Elsevier; 2007.

[48] Kasperovich G, Hausmann J. Improvement of fatigue resistance and ductility of TiAl6V4 processed by selective laser melting. J Mater Process Technol 2015;220: 202–14. https://doi.org/10.1016/j.jmatprotec.2015.01.025.

[49] Timošenko SP, Goodier JN. Theory of elasticity. 3. ed. Auckland: McGraw-Hill; 2004.

[50] Taylor David. Geometrical effects in fatigue: a unifying theoretical model. Int J Fatigue 1999;21(5):413–20. https://doi.org/10.1016/S0142-1123(99)00007-9.

[51] Tammas-Williams S. XCT analysis of the defect distribution and its effect on the static and dynamic mechanical properties of Ti-6Al-4V components manufactured by electron beam additive manufacture. University of Manchester 2016.

[52] Schönbauer BM, Mayer H. Effect of small defects on the fatigue strength of martensitic stainless steels. Int J Fatigue 2019;127:362–75. https://doi.org/10.1016/j.ijfatigue.2019.06.021.

[53] British Standards Institution. BS 7910: Guide to methods for assessing the acceptability of flaws in metallic structures. London: BSI 2007.

[54] Pilkey WD, Pilkey DF, Peterson RE. Peterson's stress concentration factors. 3rd ed. Hoboken, N.J: John Wiley; 2008.

[55] Mura T. In: Micromechanics of defects in solids. Dordrecht Netherlands: Springer; 1987. https://doi.org/10.1007/978-94-009-3489-4.

[56] Schijve J, editor. Fatigue of Structures and Materials. Dordrecht: Springer Netherlands 2009. https://doi.org/10.1007/978-1-4020-6808-9.

[57] Schneider CRA, Maddox SJ. Best practice guide on statistical analysis of fatigue data. International Institute of Welding, IIW-XIII-WG1-114-03 2003.

[58] Lanning D, Nicholas T, Haritos G. On the use of critical distance theories for the prediction of the high cycle fatigue limit stress in notched Ti-6Al-4V. Int J Fatigue 2005;27:45–57. https://doi.org/10.1016/j.ijfatigue.2004.06.002.